Journal Pre-proofs

Densified MoS_2/Ti_3C_2 films with balanced porosity for ultrahigh volumetric capacity sodium-ion battery

Kun Ma, Yuru Dong, Hao Jiang, Yanjie Hu, Petr Saha, Chunzhong Li

PII: S1385-8947(20)33603-2
DOI: https://doi.org/10.1016/j.cej.2020.127479
Reference: CEJ 127479

To appear in: *Chemical Engineering Journal*

Received Date: 21 August 2020
Revised Date: 9 October 2020
Accepted Date: 19 October 2020

Please cite this article as: K. Ma, Y. Dong, H. Jiang, Y. Hu, P. Saha, C. Li, Densified MoS_2/Ti_3C_2 films with balanced porosity for ultrahigh volumetric capacity sodium-ion battery, *Chemical Engineering Journal* (2020), doi: https://doi.org/10.1016/j.cej.2020.127479

Densified MoS_2/Ti_3C_2 films with balanced porosity for ultrahigh volumetric capacity sodium-ion battery

Kun Ma[a], Yuru Dong[a], Hao Jiang[a], Yanjie Hu[a], Petr Saha[b], Chunzhong Li*[a]*

[a] Key Laboratory for Ultrafine Materials of Ministry of Education, Shanghai Engineering Research Center of Hierarchical Nanomaterials, School of Materials Science and Engineering, East China University of Science and Technology, Shanghai 200237, China.

[b] Centre of Polymer Systems, University Institute, Tomas Bata University in Zlin, Trida T. Bati 5678, 760 01 Zlin, Czech Republic.

E-mail: jianghao@ecust.edu.cn (Prof. H. Jiang), czli@ecust.edu.cn (Prof. C. Z. Li).

Abstract

Developing high volumetric energy density sodium-ion batteries (SIBs) is indispensable for catering to the miniaturization and flexibility of various consumer electronics. Herein, we have reported the flexible and compact MoS_2/Ti_3C_2 hybrid films with balanced porosity, where the few-layered MoS_2 nanosheets are parallelly intercalated into the Ti_3C_2 interlayer space in virtue of strong electrostatic effect and difference in their sizes. The hybrid films have been stabilized by the two-dimensional (2D) confinement effect and the Ti-S-Mo bonds with a high density of ~ 2.9 g cm^{-3}. Furthermore, the dual 2D compounds intrinsically possess satisfied ions conductivity, and meanwhile give rapid electrons transfer after assembling such superstructure. When directly used as SIB anode, the MoS_2/Ti_3C_2 hybrid films deliver an exceptional volumetric specific capacity of 1510 mAh cm^{-3} at 0.28 mA cm^{-2} and 650 mAh cm^{-3} at 14 mA cm^{-2}. The specific capacity remains unchanged after 300 cycles at 1.4 mA cm^{-2}. More significantly, the areal specific capacity shows a linear relationship with the increase of film thickness from 9.6 to 43.1 μm without sacrificing the volumetric capacity.

Keywords: MXene, compact film, MoS_2, volumetric capacity, Na-ion battery

1. Introduction

Exploiting high volumetric energy density sodium-ion batteries (SIBs) is extremely urgent in view of the miniaturization and flexibility trend of various electronic gizmos, and prominent cost efficiency and superior safety of sodium compared with lithium [1-4]. Nevertheless, the larger volume of Na^+ than Li^+ and unsatisfied kinetics limit paces to develop versatile electrode materials featured by high-efficiency and reversible Na^+ intercalation/de-intercalation [5,6]. As a new 2D material class, high-density MXenes with rich terminal groups and superior conductivity have a great potential for decent volumetric energy storage [7-9]. However, their pseudocapacitance-type sodium storage behavior usually results in an unsatisfactory output capacity (< 450 mAh cm^{-3}) [10-12]. Of late, 2D metal chalcogenide materials (2D-MSs) have focused the continuous concerns on sodium storage and green energy because of their featured laminar structure, large nanospace and high theoretical volumetric capacity (*e.g.* 3216 mAh cm^{-3} for MoS_2) [13-16]. In particular, the nano-sized 2D-MSs with the shortened electron/ion transport distance and highly exposed Na^+ storage sites usually possess a higher practical capacity [17,18]. In this regard, constructing nano-sized 2D-MSs/MXenes hybrids is very conducive to improving the sodium storage capability of MXene-based materials.

Mixing MXenes with nano-sized 2D-MSs has been regarded as the most direct strategy for building 2D-MSs/MXene composites (**Fig. 1a**) [19-21]. For example, Zhang et al. prepared a SnS_2/MXene nanocomposite by simply mixing few-layered SnS_2 and exfoliated MXene nanosheets, exhibiting the enhanced electrochemical performance [19]. Unfortunately, the weak contact and disordered arrangement between two components tremendously hinder the electron/ion transport along with inferior rate capability and

meanwhile cause the poor stability. Recently, intercalating 2D-MSs species into MXene interlayers has attracted keen interest owing to the unique confinement effect and elaborate coupling between components (**Fig. 1b**) [22-24]. For example, our group designed a MoS_2-in-Ti_3C_2 hybrid where few-layered MoS_2 nanocrystals vertically pillared Ti_3C_2 layers, showing a high gravimetric specific capacity and excellent structural stability [22]. Nevertheless, the vertical nanocrystals create overmuch pores and high specific surface area, which inevitably decrease the densification of composites and hence trigger an inferior volumetric performance. Summarized from the design concept of above nanostructures, we can infer that the plane-to-plane architecture with balanced porosity will endow electrode materials with the compact structure and the appropriate ion migration path (**Fig. 1c**), which is expected to simultaneously obtain high volumetric/gravimetric capacity and rapid reaction kinetics. However, it is still challenging to synthesize the plane-to-plane MSs/MXene based hybrids and achieve the trade-off between porosity and densification.

Herein, we have proposed the design of a flexible and dense MoS_2/Ti_3C_2 hybrid films with balanced porosity, in which the few-layered MoS_2 nanosheets are intercalated into the Ti_3C_2 interspaces parallelly with the help of strong electrostatic effect and difference in their sizes. The balanced compaction and porosity not only can significantly increase the tap density of film to ~ 2.9 g cm^{-3}, but also guaranty complete electrolyte wetting and fast ion diffusion. Moreover, the films have been stabilized by the 2D confinement effect and the tight Ti-S-Mo bonds. Furthermore, such dual 2D components with large interlayer space intrinsically possess satisfied ions conductivity, and meanwhile assembled superstructures give rapid electrons transfer. When directly used as anodes for SIB, the MoS_2/Ti_3C_2 hybrid films contribute exceptional volumetric capacity of 1510 mAh cm^{-3} at 0.28 mA cm^{-2} and 650

mAh cm^{-3} even at 14 mA cm^{-2}, which vastly outperform those of MoS_2/Ti_3C_2 mixture films (770 mAh cm^{-3} at 0.28 mA cm^{-2}/280 mAh cm^{-3} at 14 mA cm^{-2}). Additionally, the hybrid films also show a prolonged life-span of 300 cycles at 1.4 mA cm^{-2}. More impressively, the areal specific capacity can be linearly tuned up to 4.3 mAh cm^{-2} as the film thickness increases from 9.6 to 43.1 μm without sacrificing the volumetric capacity.

2. Experimental Section

2.1 Preparation of the PDDA modified Ti_3C_2 nanosheets and the exfoliated MoS_2 nanosheets

The exfoliated Ti_3C_2 (E-Ti_3C_2) nanosheets were firstly prepared by selectively etching Al in Ti_3AlC_2 and subsequent ultrasonic treatment. Specifically, 2 g of LiF powder (Energy Chemical) were dissolved in the mixture solution of HCl (16 mL) and deionized (DI) water (4 mL). Then, 2 g of Ti_3AlC_2 (Forsman Technology Co., Ltd.) were poured into the above solution in batches before stirring for 24 h at 40 °C. Afterward, the solid residue was washed by DI water, then dispersed in DI water (400 mL) and treated with probe-ultrasonic using JYD-900L instrument for 10 min with a pulse of 8 s on and 2 s off in Ar atmosphere. Thereafter, the supernatant that experienced centrifugation at 3000 rpm for 45 min was further centrifuged for another 45 min at 8000 rpm to collect large E-Ti_3C_2 precipitants. The small E-Ti_3C_2 can be realized by further treating the large Ti_3C_2 NSs dispersion with probe-ultrasonic for 30 min in Ar atmosphere. Finally, the PDDA (Adamas-beta, average molecular weight is 100 000-200 000) modified Ti_3C_2 (~1.0 mg mL^{-1}) was obtained via re-dispersing the above precipitates into 0.05 wt% PDDA solution.

The exfoliated MoS_2 (E-MoS_2) nanosheets were gained based on the previous literature with a minor modification [25]. Specifically, the solid MoS_2 powder (1 g, Sigma-Aldrich) was

dispersed in 200 mL of sodium deoxycholate solution (2 mg mL^{-1}) and then stirred for 60 min. The mixed solution was treated by probe-ultrasonic for 8 h with a pulse of 6 s on and 4 s off. After centrifugation at 1500 rpm for 80 min, the supernatant was collected and further centrifuged at 6000 rpm for another 80 min. Afterwards, the sediments were washed with DI water thrice. Finally, the E-MoS_2 (~1.0 mg mL^{-1}) suspension was obtained by re-dispersing above precipitates into DI water.

2.2 Preparation of the MoS_2/Ti_3C_2 hybrid films

100 mL of E-MoS_2 dispersed solution were dropped into the 50 mL of PDDA modified Ti_3C_2 suspension under stirring, then standing for 1 h. Afterwards, the as-generated MoS_2/Ti_3C_2 agglomerates settled to the bottom. Finally, the flexible and compact MoS_2/Ti_3C_2 hybrid films were obtained by vacuum filtering MoS_2/Ti_3C_2 sediment with subsequent freeze-drying procedure. The thicknesses of films can be regulated by changing the amount of filtered solutions. As controls, the MoS_2/Ti_3C_2 mixture films were prepared via directly filtering mixture solution of E-MoS_2 and E-Ti_3C_2 free of PDDA decoration. Pure Ti_3C_2 films were also synthesized by filtering the E-Ti_3C_2 solution.

2.3 Characterization

The product X-ray diffraction (XRD) analyses were executed employing a Bruker D8 Advance X-ray diffractometer with Cu Ka radiation. The structural morphology was investigated using field-emission scanning electron microscope (FESEM, Hitachi S-4800) and transmission electron microscope (TEM, JEOL-2100). The X-ray photoelectron spectroscopy (XPS, Bruker RFS 100/S spectrometer, 532 nm laser beam) spectra were characterized to acquired surface compositions and element valence of products. Nitrogen adsorption/desorption curves were taken on a Micromeritcs ASAP 2010

Brunauer-Emmett-Teller (BET) measurement analyzer.

2.4 Electrochemical Measurements

Electrochemical performances were investigated by applying coin-type 2032 half cells, which were integrated in a glove box filled with argon. The resultant free-standing films were directly as working electrode. The counter electrode was Na foil, and the separator that we chose was Whatman GF/D. The 1.0 M $NaPF_6$ in dimethoxyethane (DME) was applied as the electrolyte. Cyclic voladtammetry (CV) experiments were implement on an Autolab PGSTAT302N at different sweep speeds from 0.2 to 1.0 mV s^{-1}. Galvanostatic charge/discharge results were recorded on a LANDCT2001A battery tester in the thermotank (25 °C). The galvanostatic intermittent titration technique (GITT) technology was also implemented on aforesaid battery tester with a test pulse of charging and discharging at 100 mA g^{-1} for 15 min and break for 1 h.

3. Results and discussion

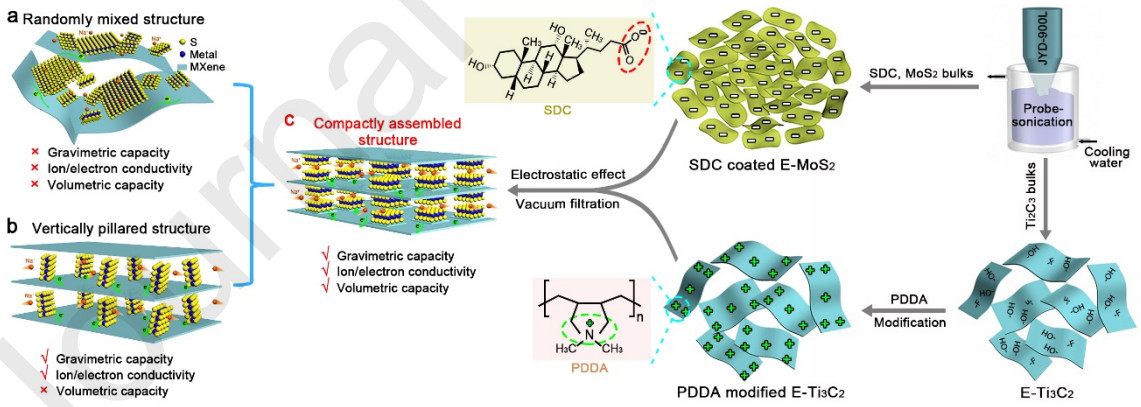

Fig. 1 The design concept and synthesis process of electrode materials for SIBs with high volumetric and gravimetric capacity.

The fabrication procedure of the compact MoS_2/Ti_3C_2 hybrid films is illustrated in **Fig. 1**. Specifically, the exfoliated Ti_3C_2 nanosheets (E-Ti_3C_2 NSs) and exfoliated MoS_2

nanosheets (E-MoS_2 NSs) were firstly prepared by different delaminated process, whose morphology features are shown in **Fig. S1**. The E-MoS_2 NSs possess a size of several micrometers and a few-layer lateral feature, while E-MoS_2 NSs also have the few-layer structure with a 200 nm size. The big size difference between E-MoS_2 and E-Ti_3C_2 NSs guarantees the feasibility of balancing porosity and densification of the MoS_2/Ti_3C_2 superstructures. The detailed demonstration and discussion will be executed later. Then, the sodium deoxycholate (SDC) surfactant coated E-MoS_2 NSs solution with a zeta potential of -28 mV (**Fig. S2**) was dropped into the positively PDDA-modified Ti_3C_2 NSs suspension (59 mV). Afterwards, the MoS_2/Ti_3C_2 hybrids generated and settled down to the bottom (right of **Fig. S3**) because of strong electrostatic interaction. Finally, the flexible and compact MoS_2/Ti_3C_2 hybrid films can be obtained by filtering above precipitation, in which the few-layered MoS_2 NSs were parallelly intercalated into Ti_3C_2 interlayers. As a control, the MoS_2/Ti_3C_2 mixture film was synthesized via simple physical mixture of MoS_2 and Ti_3C_2 free of PDDA decoration. The MoS_2 content in the mixture film is 65% according to the inductively coupled plasma result.

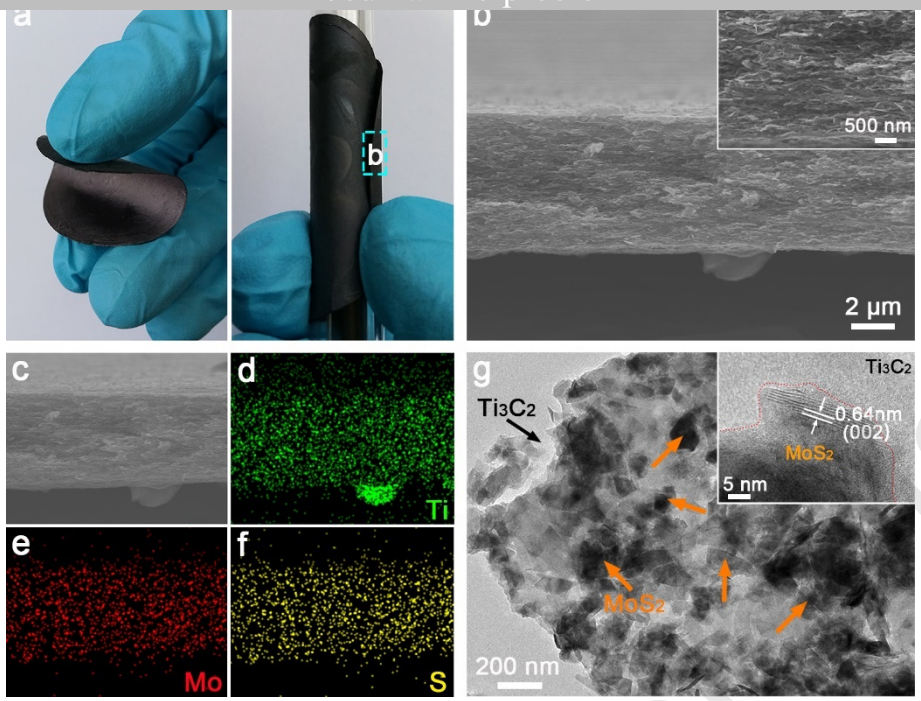

Fig. 2 (a) Photos, (b) cross-section SEM images (inset: enlarged corresponding SEM images), and (c-f) SEM-EDS mapping of the flexible and compact MoS_2/Ti_3C_2 hybrid films. (g) TEM image of the MoS_2/Ti_3C_2 hybrid films (inset: enlarged corresponding HRTEM image).

As revealed in **Fig. 2a** and **Fig. S4**, the MoS_2/Ti_3C_2 hybrid films exhibit the prominent flexibility and mechanical strength with a high and stable conductivity of ~47 S cm^{-1} during repeated 500 bending cycles, which is much higher than ~14 S cm^{-1} of the control sample. Further, the cross-section morphologies of the flexible MoS_2/Ti_3C_2 hybrid films are observed in **Fig. 2b**. Such films demonstrate a regular plane-to-plane dense structure with more moderate pores than pure Ti_3C_2 films (**Fig. S5**), which can facilitate the electrolyte infiltration and ion diffusion. In addition, the homogeneous element distribution (**Fig. 2c-f**) also proves the uniform and orderly assembly of the MoS_2 and Ti_3C_2 NSs in the MoS_2/Ti_3C_2 hybrid films. Interestingly, even when the thickness is amplified to ~43 μm, the hybrid films still exhibit a high compactness while the MoS_2/Ti_3C_2 mixture films show a loose morphology with the

random arrangement of nanosheets and excess pores owing to electrostatic repulsion (**Fig. S6**). Specifically, even after ultrasonic treatment for 30 min, the MoS_2/Ti_3C_2 hybrid films keep an intact compact morphology profiting from the strong electrostatic interaction and chemical interface coupling between two components. However, the MoS_2 NSs in MoS_2/Ti_3C_2 mixture films randomly distribute on Ti_3C_2 surface with obvious folds resulting from the weak combination between E-MoS_2 and E-Ti_3C_2 NSs (**Fig. S7**). To further reveal the importance of the difference in nanosheet sizes in assembling the compact MoS_2/Ti_3C_2 superstructures. The small Ti_3C_2 (S-Ti_3C_2) NSs with a size of ~ 200 nm are first prepared and shown in **Fig. S8a**. Then, the loose and rigid MoS_2/S-Ti_3C_2 hybrid films with a low density of ~1.5 g cm^{-3} can be obtained via compositing MoS_2 NSs and PDDA modified S-Ti_3C_2 NSs (**Fig. S8c-d**). The specific interpretation can be visualized by the schematic in **Fig. S9**. Obviously, the reduced size inevitably increases the surface energy of materials, which aggravates the tendency of self-aggregation and counteracts the electrostatic effect between two components, thus resulting in random combination of the nanosheets. The TEM images of **Fig. 2g** further provide the microstructure detail of the MoS_2/Ti_3C_2 hybrid films, where few-layered and small-sized MoS_2 NSs are evenly and parallelly distributed on the surface of micron-sized Ti_3C_2 substrates. This plane-to-plane design concept achieves a highly compact combination of MoS_2 and Ti_3C_2, which can contribute to high volumetric capacity.

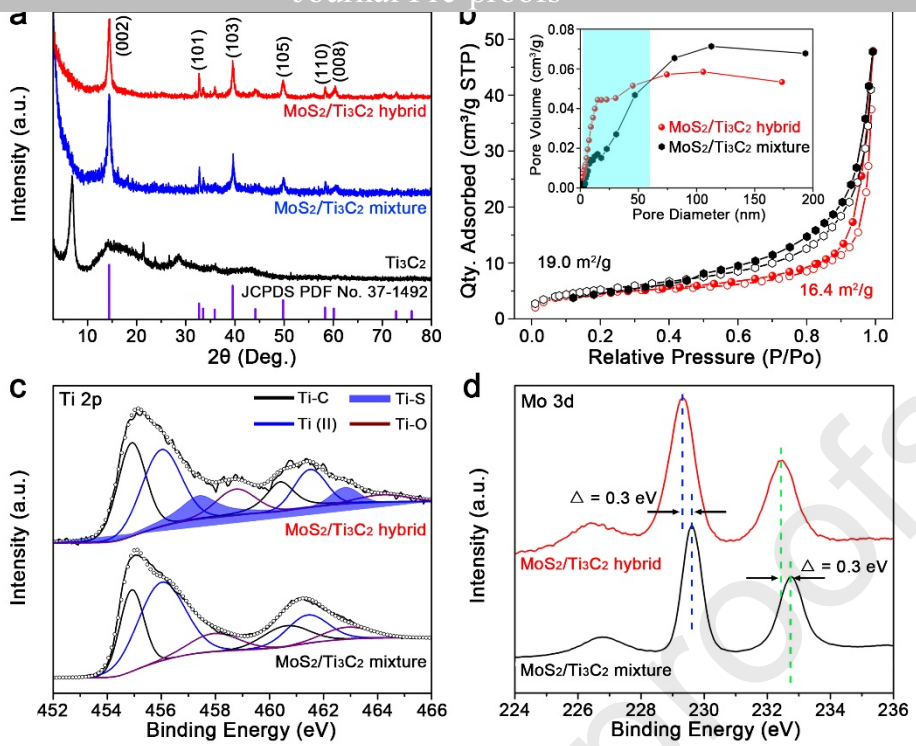

Fig. 3 (a) XRD patterns of the Ti_3C_2 films, the MoS_2/Ti_3C_2 mixture films and the MoS_2/Ti_3C_2 hybrid films. (b) Nitrogen adsorption-desorption isotherms (the inset is the corresponding pore structure distribution). (c) High-resolution Ti 2p spectra and (d) Mo 3d spectra of the MoS_2/Ti_3C_2 mixture films and the MoS_2/Ti_3C_2 hybrid films.

The crystal structure of the as-prepared samples was revealed by X-ray powder diffraction (XRD). As demonstrated in **Fig. 3a**, the (002) peak of Ti_3C_2 is absent in both MoS_2/Ti_3C_2 hybrid films and MoS_2/Ti_3C_2 mixture films, suggesting the single-layer structure of Ti_3C_2 NSs [26]. Furthermore, the weakening of the MoS_2 (002) peak in MoS_2/Ti_3C_2 hybrid film can be proved by the intensity ratio of (002)/(103) peaks. The smaller ratio of the MoS_2/Ti_3C_2 hybrid film than MoS_2/Ti_3C_2 mixture film indicates that the self-agglomeration of MoS_2 in the hybrid film has been effectively suppressed [27]. Notably, because of the ordered and compact assembly, the MoS_2/Ti_3C_2 hybrid films show a slightly reduced specific surface area compared to MoS_2/Ti_3C_2 mixture films (**Fig. 3b**). Meanwhile, the MoS_2/Ti_3C_2 hybrid

films have a richer and more balanced pore distribution dominated by 10-50 nm mesopores while the pores of MoS_2/Ti_3C_2 mixture films are mainly distributed over 100 nm (inset of **Fig. 3b**). The balanced porosity can significantly improve the material tap density and meantime guaranty complete electrolyte wetting and fast ion diffusion, which can propel a high volumetric capacity and rapid reaction kinetics. The surface electronic states and chemical structure of the films were further researched through employing X-ray photoelectron spectroscopy (XPS) analyses. The Ti 2p spectra for MoS_2/Ti_3C_2 hybrid films and MoS_2/Ti_3C_2 mixture films are shown in **Fig. 3c**. It is notable that two small peaks at 457.4/462.8 eV belonging to Ti-S-Mo bond [28], are observed in the MoS_2/Ti_3C_2 hybrid films while disappearing in the MoS_2/Ti_3C_2 mixture films. Meantime, a 0.3 eV shift to low binding energy of both Mo 3d and S 2p peak positions can be seen in the MoS_2/Ti_3C_2 hybrid films compared with the MoS_2/Ti_3C_2 mixture films (**Fig. 3d** and **Fig. S10**), further corroborating the strong interface coupling [22,29]. Such strong covalent bonds not only effectively mitigate the nanosheet self-agglomeration to stabilize the hybrid films, but also can be applied as the electron bridge at the MoS_2/Ti_3C_2 heterointerfaces.

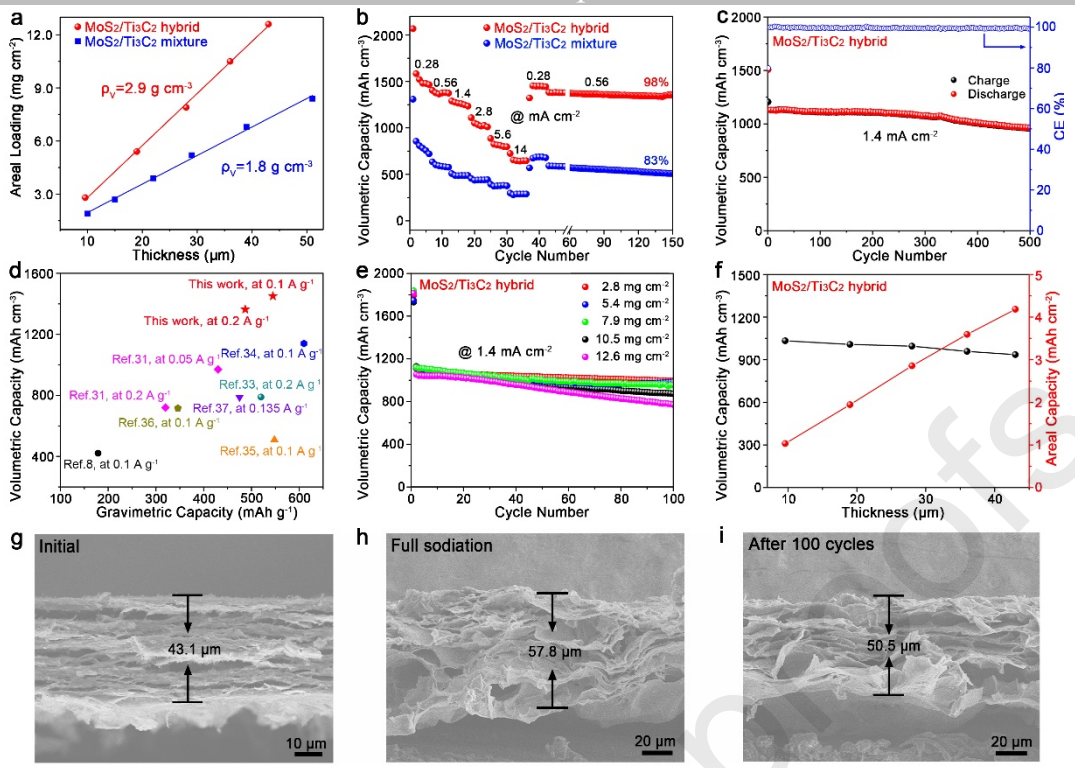

Fig. 4 (a) Thickness versus areal loading plot for the MoS_2/Ti_3C_2 hybrid films. (b) Rate performance of the MoS_2/Ti_3C_2 mixture films and the MoS_2/Ti_3C_2 hybrid films at 2.8 mg cm^{-2}. (c) The long-term cycle at 1.4 mA cm^{-2} of the MoS_2/Ti_3C_2 hybrid films at 2.8 mg cm^{-2}. (d) Comparison of gravimetric and areal capacities of recently reported anode materials for SIBs. (e) Cycling stability at 1.4 mA cm^{-2} of the MoS_2/Ti_3C_2 hybrid films with different areal loading. (f) Volumetric and areal capacities at 1.4 mA cm^{-2} of the MoS_2/Ti_3C_2 hybrid films versus thickness. (g-i) SEM images of the MoS_2/Ti_3C_2 hybrid films at 12.6 mg cm^{-2} for different sodiation states.

The sodium storage capabilities of the MoS_2/Ti_3C_2 hybrid films with different MoS_2 content were firstly examined in coin-type 2032 cells (**Fig. S11**). The MoS_2/Ti_3C_2 hybrid films can be straightway applied as work electrode free of conductive agent and binder. The as-optimized films with 67 wt% MoS_2 content show the highest discharging capacity at every

current density compared to the MoS_2/Ti_3C_2 film with MoS_2 content as low as 50 wt% (L-MoS_2/Ti_3C_2) and the MoS_2/Ti_3C_2 film with high MoS_2 content of 74 wt% (H-MoS_2/Ti_3C_2). Impressively, the areal loading of the optimized MoS_2/Ti_3C_2 hybrid films can be linearly regulated from 2.8 to 12.6 mg cm^{-2} with the thickness range of 9.6 to 43.1 μm only by controlling volume of the filtered solutions (**Fig. 4a**). The volumetric density of the hybrid films is then calculated to be ~2.9 g cm^{-3}, which is significantly higher than 1.8 g cm^{-3} of the MoS_2/Ti_3C_2 mixture films and most of electrode materials in the reported literatures [30-33]. Then, the capacity retention of the MoS_2/Ti_3C_2 hybrid films at 2.8 mg cm^{-2} was evaluated at areal current densities from 0.28 mA cm^{-2} to 14 mA cm^{-2} (**Fig. 4b**). The MoS_2/Ti_3C_2 hybrid films deliver an exceptional volumetric capacity of 1510 mAh cm^{-3} with an initial Coulombic efficiency of ~ 68.4% at 0.28 mA cm^{-2} corresponding to a fascinating gravimetric specific capacity of 540 mAh g^{-1} (**Fig. S12**), which is far superior than the MoS_2/Ti_3C_2 mixture films (770 mAh cm^{-3}/420 mAh g^{-1}). Inspiringly, an outstanding capacity of 650 mAh cm^{-3} is still gained even at the high current of 14 mA cm^{-2}. As measured again at 0.28 mA cm^{-2}, the MoS_2/Ti_3C_2 hybrid films can maintain an average specific capacity of 1450 mAh cm^{-3}. Moreover, the films also control a decent cycling capability. The discharge capacity of 1360 mAh cm^{-3} is achieved with only 2% capacity attenuation after prolonged 100 cycles at 0.56 mA cm^{-2}. The superior performance can be attributed to the decent ion/electron migration and robust structure, which is caused by the large intrinsic interlayers of 2D components, tight chemical interface interaction, and unique 2D confinement effect. As displayed in **Fig. 4c**, the MoS_2/Ti_3C_2 hybrid films still contribute a specific capacity of 970 mAh cm^{-3} even after 500 cycles at 1.4 mA cm^{-2}. For all we know, such excellent volumetric capacity is almost the best report for free-standing electrode materials for SIBs [8,31,33-37]. An overall comparison is

shown in **Fig. 4d**. To further clarify effect of the areal loading on electrochemical properties, the capacity retention of MoS_2/Ti_3C_2 hybrid films with various thicknesses are also investigated. As provided in **Fig. 4e**, all the MoS_2/Ti_3C_2 hybrid films do not show visible capacity loss after 100 cycles until the areal loading is above 10.5 mg cm^{-2}. The volumetric and areal capacities versus thicknesses were further demonstrated in **Fig. 4f**. As the increase of thickness, the volumetric capacity is almost constant at 1.4 mA cm^{-2} with the linear increasing of areal capacity from 1.1 to 4.3 mAh cm^{-2}. Further, the cross-section morphologies of the MoS_2/Ti_3C_2 hybrid films with a maximum areal loading of 12.6 mg cm^{-2} at disparate charging/discharging states are also shown in the **Fig. 4g-i**. After the first full sodiation, there is a visible expansion from 43.1 to 57.8 μm in the hybrid film because of the Na^+ intercalation and inevitable swelling effect caused by electrolyte infiltration. Impressively, even after 100 cycles, the compact structure of hybrid film is still well-maintained with a moderate thickness increase of ~17%, verifying a high structural stability. The Ti 2p spectrum after cycles also confirms the existence of Ti-S-Mo covalent bonds (**Fig. S13**), indicating the stable chemical interface coupling in the MoS_2/Ti_3C_2 hybrid films. As displayed in **Fig. S14**, due to the swelling effect and the weak combination between nanosheets, the thickness of the MoS_2/Ti_3C_2 mixture films expands from 52.0 to 208.2 μm with the obvious cracks and aggregates.

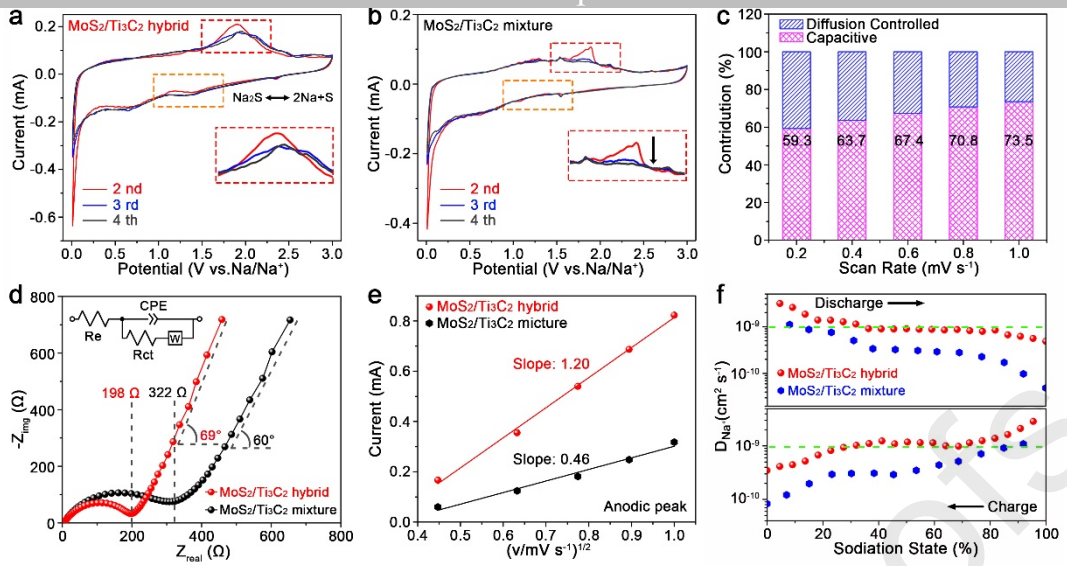

Fig. 5 (a,b) The initial four CV curves of the MoS_2/Ti_3C_2 mixture films and the MoS_2/Ti_3C_2 hybrid films at 0.2 mV s^{-1}, respectively. (c) Normalized capacitive and diffusion-controlled capacities contribution at different sweep rates of the MoS_2/Ti_3C_2 hybrid films. (d) Electrochemical impedance spectra, (e) linear relationship of the peak current (ip) *versus* the square root of the scan rate ($v^{1/2}$), and (f) Na-ion diffusion coefficient under discharge and charge states of the MoS_2/Ti_3C_2 mixture films and the MoS_2/Ti_3C_2 hybrid films.

To gain an insight into the essence of such admirable sodium storage performance, the first cyclic voltammograms (CV) in 0.01-3 V at 0.2 mV s^{-1} of two products were summarized in **Fig. S15**. In the first scanning, two products reveal the similar outline, which indicates that both have the same electrochemical reaction process. In particular, the MoS_2/Ti_3C_2 hybrid electrode possesses stronger current intensity, representing higher specific capacity. Notably, during the following three laps (**Fig. 5a,b**), the MoS_2/Ti_3C_2 hybrid electrode reveals two visible and stable peaks at 1.36/1.91 V belonging to the generation and decomposition of Na_2S, respectively [38,39]. In contrast, these two peaks in the MoS_2/Ti_3C_2 mixture electrode continue to weaken until disappear in the fourth circle. That comparison shows that the

MoS_2/Ti_3C_2 hybrid films control a good reversibility, which is mainly because of the strong chemical bonding and unique 2D confinement effect in the MoS_2/Ti_3C_2 hybrid films. The reaction kinetics of the MoS_2/Ti_3C_2 hybrid electrode was further investigated by the CV results at various test rates from 0.2 to 1.0 mV s^{-1} (**Fig. S16a**). The detailed charge storage process can be qualitatively analyzed through a logarithmic equation of $\log i = b \log v + log\ a$ [40], where a and b are variable value, v is scan rate and i represents measured current. The b value of 0.5 or 1.0 usually means diffusion-dominated reaction or surface-controlled reaction, respectively. **Fig. S16b** exhibits the MoS_2/Ti_3C_2 hybrid electrode has the high b values for both the anode (0.88) and cathode (0.91), indicating the electrochemical process is principally surface-controlled, which corresponds to fast kinetics of capacitive storage. The capacitive ratios are calculated by splitting the measured current i into capacitive-dominated process (k_1v) and the diffusion-dominated process ($k_2v^{1/2}$) based on following equation [22,41]:

$$i = k_1v + k_2v^{1/2}$$

By assuming k_1 and k_2 constants, we can determine the contribution ratios of capacitive and diffusion-controlled capacities. As exhibited in **Fig. 5c**, the capacitive ratio gradually enlarges upon the increasing of scanning rate from 0.2 to 1.0 mV s^{-1}. The capacitive reaction almost regulates the entire sodium storage with the 73.5% proportion at 1.0 mV s^{-1} (**Fig. S17**). That high pseudocapacitance contribution can ensure more and faster Na^+ storages. Furthermore, the electrochemical impedance spectra were executed and provided in **Fig. 5d**. Clearly, the MoS_2/Ti_3C_2 hybrid films possess the smaller charge transfer resistance (198 Ω *vs.* 322 Ω of MoS_2/Ti_3C_2 mixture films) with a larger slope at low frequencies, demonstrating the better electron migration kinetics and improved Na^+ transfer rates, which guarantee the high pseudocapacitance proportion. Electrochemical impedance spectra of the MoS_2/Ti_3C_2 hybrid

films with different areal loading are also shown into **Fig. S18**. The detailed comparison of charge and ion transfer ability of the different MoS_2/Ti_3C_2 hybrid films and the MoS_2/Ti_3C_2 mixture film has also been summarized in **Table S1**. Based on CV results of **Fig. S16a** and **Fig. S19a**, the Na^+ diffusion kinetics of two products are further evaluated using the Randles-Sevcik equation [42]. The MoS_2/Ti_3C_2 hybrid films display more larger slope values than the MoS_2/Ti_3C_2 mixture films (**Fig. 5e** and **Fig. S19b**), suggesting the MoS_2/Ti_3C_2 hybrid films manage the faster ion diffusion reaction. The galvanostatic intermittent titration technique (GITT) are also used to quantify Na ion diffusivity (**Fig. S20**). As provided in **Fig. 5f**, the D_{Na^+} values for the MoS_2/Ti_3C_2 hybrid films at various sodiation/desodiation stages spread over a range of ~ 10^{-9}-10^{-10} cm s^{-1}, which are greatly higher than the MoS_2/Ti_3C_2 mixture films and other anode materials for SIBs [43,44]. In consequence, it is very persuasive that such high conversion reversibility and rapid electron/ion transfer dynamics account for excellent electrochemical properties of the MoS_2/Ti_3C_2 hybrid films.

4. Conclusions

In conclusion, we have designed a flexible and compact MoS_2/Ti_3C_2 films with balanced porosity, in which the few-layered MoS_2 nanosheets are parallelly intercalated into Ti_3C_2 interlayer space due to strong electrostatic effect and difference in nanosheet sizes. The optimized porosity and densification endow the hybrid films with a high density of ~ 2.9 g cm^{-3} and the appropriate ion migration paths. Besides, the hybrid films have been stabilized by the unusual 2D confinement effect and tight Ti-S-Mo bonds. More importantly, the dual 2D components with large interlayer distance intrinsically possesses satisfied ions conductivity, and meanwhile delivers rapid electron transfer after assembling superstructures. These peculiarities can guarantee the high volumetric sodium-ion storage of the MoS_2/Ti_3C_2

compact films. When directly applied as SIB anode, the MoS_2/Ti_3C_2 hybrid films show a superhigh volumetric capacity of 1510 mAh cm^{-3} at 0.28 mA cm^{-2} and 650 mAh cm^{-3} at 14 mA cm^{-2}, which are far superior to 770 mAh cm^{-3} at 0.28 mA cm^{-2} and 280 mAh cm^{-3} at 14 mA cm^{-2} of MoS_2/Ti_3C_2 mixture films. Even after 300 cycles at 1.4 mA cm^{-2}, the compact films still contribute a specific capacity of 1080 mAh cm^{-3} with a 96% retention. Impressively, the areal specific capacity can be linearly tuned from 1.1 to 4.3 mAh cm^{-2} without obvious volumetric capacity recession. This proposal provides a new insight on engineering the microstructure of 2D materials to achieve high volumetric energy storage.

Acknowledgements

This work was supported by the National Natural Science Foundation of China (21975074 and 21838003), the Basic Research Program of Shanghai (17JC1402300), the Shanghai Scientific and Technological Innovation Project (18JC1410500), and the Fundamental Research Funds for the Central Universities (222201718002).

Appendix A. Supplementary data

Supplementary data related to this article can be found at http://www.elsevier.com/

References

[1] T. Liu, Y. Zhang, Z. Jiang, X. Zeng, J. Ji, Z. Li, X. Gao, M. Sun, Z. Lin, M. Ling, J. Zheng, C. Liang. Exploring competitive features of stationary sodium ion batteries for electrochemical energy storage. Energy Environ. Sci. 12 (2019) 1512-1533.

[2] Q. Huang, K. Turcheniuk, X. Ren, A. Magasinski, A-Y. Song, Y. Xiao, D. Kim, G.

Yushin. Cycle stability of conversion-type iron fluoride lithium battery cathode at elevated temperatures in polymer electrolyte composites. Nat. Mater. 18 (2019) 1343-1349.

[3] L. Chen, H. Jiang, Y. Hu, H. Wang, C. Li, In-situ growth of ultrathin MoS_2 nanosheets on sponge-like carbon nanospheres for lithium-ion batteries, Sci. China Mater. 61 (2018) 1049-1056.

[4] W. Zhong, J. Huang, S. Liang, J. Liu, Y. Li, G. Cai, Y. Jiang, J. Liu. New prelithiated V_2O_5 superstructure for lithium-ion batteries with long cycle life and high power. ACS Energy Lett. 5 (2020) 31-38.

[5] D. A. Stevensa, J. R. Dahn. The mechanisms of lithium and sodium insertion in carbon materials. J. Electrochem. Soc. 148 (2001) A803-A811.

[6] Y. Liu, B. V. Merinova, W. A. Goddard III. Origin of low sodium capacity in graphite and generally weak substrate binding of Na and Mg among alkali and alkaline earth metals. Proc. Natl. Acad. Sci. USA 113 (2016) 3735-3739.

[7] J. Pang, R. G. Mendes, A. Bachmatiuk, L. Zhao, H. Q. Ta, T. Gemming, H. Liu, Z. Liu, M. H. Rummeli. Applications of 2D MXenes in energy conversion and storage systems. Chem. Soc. Rev. 48 (2019) 72-133.

[8] M. R. Lukatskaya, O. Mashtalir, C. E. Ren, Y. Dall'Agnese, P. Rozier, P. L. Taberna, M. Naguib, P. Simon, M. W. Barsoum, Y. Gogotsi. Cation intercalation and high volumetric capacitance of two-dimensional titanium carbide. Science 341 (2013) 1502-1505.

[9] Y. Xia, T. S. Mathis, M-Q. Zhao, B. Anasori, A. Dang, Z. Zhou, H. Cho, Y. Gogotsi S. Yang. Thickness-independent capacitance of vertically aligned liquid-crystalline MXenes. Nature 557 (2018) 409-412.

[10] X. Xie, M. Q. Zhao, B. Anasori, K. Maleski, C. E. Ren, J. Li, B. W. Byles, E. Pomerantseva, G. Wang, Y. Gogotsi. Porous heterostructured MXene/carbon nanotube composite paper with high volumetric capacity for sodium-based energy storage devices. Nano Energy 26 (2016) 513-523.

[11] X. Xie, K. Kretschmer, B. Anasori, B. Sun, G. Wang, Y. Gogotsi. Porous $Ti_3C_2T_x$ MXene for ultrahigh-rate sodium-ion storage with long cycle life. ACS Appl. Nano Mater. 1 (2018) 505-511.

[12] M. Q. Zhao, X. Xie, C. E. Ren, T. Makaryan, B. Anasori, G. Wang, Y. Gogotsi. Hollow MXene spheres and 3D macroporous MXene frameworks for Na-ion storage. Adv. Mater. 29 (2017) 1702410.

[13] X. Zhang, Z. Lai, Q. Ma, H. Zhang. Novel structured transition metal dichalcogenide nanosheets. Chem. Soc. Rev. 47 (2018) 3301-3338.

[14] K. Ma, Y. Liu, H. Jiang, Y. Hu, R. Si, H. Liu, C. Li. Multivalence-ion intercalation enables ultrahigh 1T phase MoS_2 nanoflowers to enhanced sodium storage performance. CCS Chem. 2 (2020) 1472-1482.

[15] P. Li, J. Y. Jeong, B. Jin, K. Zhang, J. H. Park. Vertically oriented MoS_2 with spatially controlled geometry on nitrogenous graphene sheets for high-Performance sodium-ion batteries. Adv. Energy Mater. 8 (2018) 1703300.

[16] W. Zhong, Z. Wang, N. Gao, L. Huang, Z. Lin, Y. Liu, F. Meng, J. Deng, S. Jin, Q. Zhang, L. Gu. Coupled vacancy pairs in Ni-doped CoSe for improved electrocatalytic hydrogen production through topochemically deintercalation. Angew. Chem. Int. Ed. (2020) 10.1002/anie.202011378.

[17] Y. Liu, X. Y. Yu, Y. Fang, X. Zhu, J. Bao, X. Zhou, X. W. Lou. Confining SnS_2 ultrathin

nanosheets in hollow carbon nanostructures for efficient capacitive sodium storage. Joule 2 (2018) 725-735.

[18] Z. Miao, P. Wang, Y. Xiao, H. Fang, L. Zhen, C. Xu. Dopamine-induced formation of ultrasmall few-layer MoS_2 homogeneously embedded in N-doped carbon framework for enhanced lithium-ion storage. ACS Appl. Mater. Interfaces 8 (2016) 33741-33748.

[19] Y. Wu, P. Nie, L. Wu, H. Dou, X. Zhang. 2D MXene/SnS_2 composites as high-performance anodes for sodium ion batteries. Chem. Eng. J. 334 (2018) 932-938.

[20] X. Guo, X. Xie, S. Choi, Y. Zhao, H. Liu, C. Wang, S. Chang G. Wang. Sb_2O_3/MXene($Ti_3C_2T_x$) hybrid anode materials with enhanced performance for sodium-ion batteries. J. Mater. Chem. A 5 (2017) 12445-12452.

[21] G. Du, M. Tao, W. Gao, Y. Zhang, R. Zhan, S. Bao, M. Xu. Preparation of $MoS_2/Ti_3C_2T_x$ composite as anode material with enhanced sodium/lithium storage performance. Inorg. Chem. Front. 6 (2019) 117-125.

[22] K. Ma, H. Jiang, Y. Hu, C. Li. 2D nanospace confined synthesis of pseudocapacitance-dominated MoS_2-in-Ti_3C_2 superstructure for ultrafast and stable Li/Na-ion batteries. Adv. Funct. Mater. 28 (2018) 1804306.

[23] J. Li, L. Han, Y. Li, J. Li, G. Zhu, X. Zhang, T. Lu, L. Pan. MXene-decorated SnS_2/Sn_3S_4 hybrid as anode material for high-rate lithium-ion batteries. Chem. Eng. J. 380 (2020) 122590.

[24] H. Jiang, H. Zhang, L. Chen, Y. Hu, C. Li, Nanospace-confinement synthesis: designing high-energy electrode materials towards ultrastable lithium-ion batteries. Small 16 (2020) 2002351.

[25] Y. Liu, X. He, D. Hanlon, A. Harvey, U. Khan, Y. Li, J. N. Coleman. Electrical,

mechanical, and capacity percolation leads to high-performance MoS_2/nanotube composite lithium ion battery electrodes. ACS Nano 10 (2016) 5980-5990.

[26] X. Wu, Z. Wang, M. Yu, L. Xiu, J. Qiu. Stabilizing the MXenes by carbon nanoplating for developing hierarchical nanohybrids with efficient lithium storage and hydrogen evolution capability. Adv. Mater. 29 (2017) 1607017.

[27] Q. Pan, Q. Zhang, F. Zheng, Y. Liu, Y. Li, X. Ou, X. Xiong, C. Yang, M. Liu. Construction of MoS_2/C hierarchical tubular heterostructures for high-performance sodium ion batteries. ACS Nano 12 (2018) 12578-12586.

[28] X. Liang, A. Garsuch, L. F. Nazar. Sulfur cathodes based on conductive MXene nanosheets for high-performance lithium-sulfur batteries. Angew. Chem. Int. Ed. 54 (2015) 3907-3911.

[29] J. Luo, X. Tao, J. Zhang, Y. Xia, H. Huang, L. Zhang, Y. Gan, C. Liang, W. Zhang. Sn^{4+} ion decorated highly conductive Ti_3C_2 MXene: Promising lithium-ion anodes with enhanced volumetric capacity and cyclic performance. ACS Nano 10 (2016) 2491-2499.

[30] Y. Liu, X. He, D. Hanlon, A. Harvey, J. N. Coleman, Y. Li. Liquid phase exfoliated MoS_2 nanosheets percolated with carbon nanotubes for high volumetric/areal capacity sodium-ion batteries. ACS Nano 10 (2016) 8821-8828.

[31] X. Lu, F. Luo, Q. Xiong, H. Chi, H. Qin, Z. Ji, L. Tong, H. Pan. Sn-MOF derived bimodal-distributed SnO_2 nanosphere as a high performance anode of sodium ion batteries with high gravimetric and volumetric capacities. Mater. Res. Bull. 99 (2018) 45-51.

[32] D. C. Lin, Z. D. Lu, P. C. Hsu, H. R. Lee, N. Liu, J. Zhao, H. T. Wang, C. Liu, Y. Cui. A high tap density secondary silicon particle anode fabricated by scalable mechanical

pressing for lithium-ion batteries. Energy Environ. Sci. 8 (2015) 2371-2376.

[33] J. Ding, H. Zhou, H. Zhang, L. Tong, D. Mitlin. Selenium impregnated monolithic carbons as free-standing cathodes for high volumetric energy lithium and sodium metal batteries. Adv. Energy Mater. 8 (2018) 1701918.

[34] Z. Liu, L. Zhang, L. Sheng, Q. Zhou, T. Wei, J. Feng, Z. Fan. Edge-nitrogen-rich carbon dots pillared graphene blocks with ultrahigh volumetric/gravimetric capacities and ultralong life for sodium-ion storage. Adv. Energy Mater. 8 (2018) 1802042.

[35] H. Ye, L. Wang, S. Deng, X. Zeng, K. Nie, P. N. Duchesne, B. Wang, S. Liu, J. Zhou, F. Zhao, N. Han, P. Zhang, J. Zhong, X. Sun, Y. Li, Y. Li, J. Lu. Amorphous MoS_3 infiltrated with carbon nanotubes as an advanced anode material of sodium-ion batteries with large gravimetric, areal, and volumetric capacities. Adv. Energy Mater. 7 (2017) 1601602.

[36] Y. Liu, Y. Yang, X. Wang, Y. Dong, Y. Tang, Z. Yu, Z. Zhao, J. Qiu. Flexible paper-like free-standing electrodes by anchoring ultrafine SnS_2 nanocrystals on graphene nanoribbons for high-performance sodium ion batteries. ACS Appl. Mater. Interfaces 9 (2017) 15484-15491.

[37] D. Li, J. Zhou, X. Chen, H. Song. Graphene-loaded Bi_2Se_3: A conversion-alloying-type anode material for ultrafast gravimetric and volumetric Na storage. ACS Appl. Mater. Interfaces 10 (2018) 30379-30387.

[38] J. Wang, J. Liu, H. Yang, D. Chao, J. Yan, S. V. Savilov, J. Lin, Z. X. Shen. MoS_2 nanosheets decorated Ni_3S_2@MoS_2 coaxial nanofibers: Constructing an ideal heterostructure for enhanced Na-ion storage. Nano Energy 20 (2016) 1-10.

[39] W. Ren, W. Zhou, H. Zhang, C. Cheng. ALD TiO_2-coated flower-like MoS_2 nanosheets

on carbon cloth as sodium ion battery anode with enhanced cycling stability and rate capability. ACS Appl. Mater. Interfaces 9 (2017) 487-495.

[40] K. Yao, Z. Xu, J. Huang, M. Ma, L. Fu, X. Shen, J. Li, M. Fu. Bundled defect-rich MoS_2 for a high-rate and long-life sodium-ion battery: achieving 3D diffusion of sodium ion by vacancies to improve kinetics. Small 15 (2019) 1805405.

[41] X. Xu, R. Zhao, W. Ai, B. Chen, H. Du, L. Wu, H. Zhang, W. Huang, T. Yu. Controllable design of MoS_2 nanosheets anchored on nitrogen-doped graphene: Toward fast sodium storage by tunable pseudocapacitance. Adv. Mater. 30 (2018) 1800658.

[42] Z. Deng, H. Jiang, Y. Hu, Y. Liu, L. Zhang, H. Liu, C. Li. 3D ordered macroporous MoS_2@C nanostructure for flexible Li-ion batteries. Adv. Mater. 29 (2017) 1603020.

[43] B. Yin, X. Cao, A. Pan, Z. Luo, S. Dinesh, J. Lin, Y. Tang, S. Liang, G. Cao. Encapsulation of CoS_x nanocrystals into N/S co-doped honeycomb-like 3D porous carbon for high-performance lithium storage. Adv. Sci. 5 (2018) 1800829.

[44] Y. Li, Y. Liang, F. C. R. Hernandez, H. D. Yoo, Q. An, Y. Yao. Enhancing sodium-ion battery performance with interlayer-expanded MoS_2-PEO nanocomposites. Nano Energy 15 (2015) 453-461.

Graphic Abstract

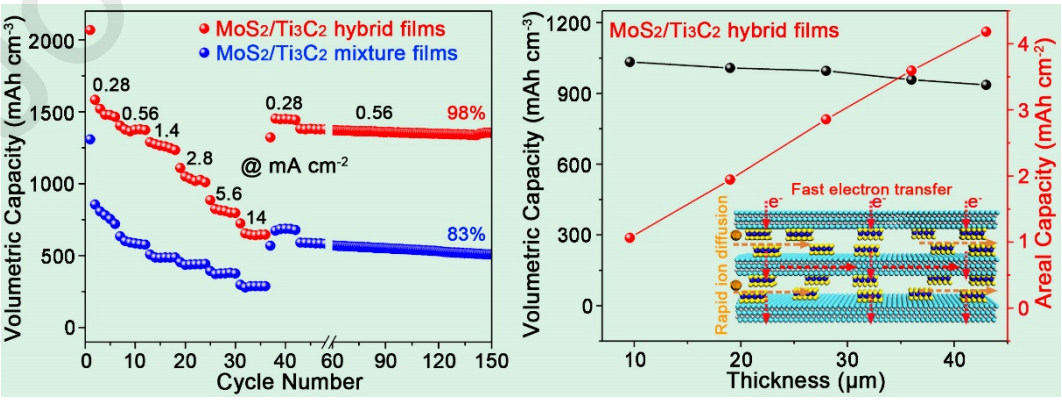

[45]

Research Highlights

1. The flexible MoS_2/Ti_3C_2 compact films with balanced porosity are reported.
2. The dense films are stabilized by the 2D confinement effect and the Ti-S-Mo bonds.
3. The superstructures with dual 2D components possess satisfied ion/electron conductivity.
4. The MoS_2/Ti_3C_2 films show a high volumetric capacity with superior rate retention.

[46]